CONCURRENT SUPERMASSIVE BLACK HOLE AND GALAXY GROWTH: LINKING ENVIRONMENT AND NUCLEAR ACTIVITY IN $z = 2.23$ Hα EMITTERS

B. D. Lehmer[1,2], A. B. Lucy[2,3], D. M. Alexander[4], P. N. Best[5], J. E. Geach[6], C. M. Harrison[4], A. E. Hornschemeier[1,2], Y. Matsuda[7], J. R. Mullaney[4], Ian Smail[8], D. Sobral[9], and A. M. Swinbank[4]

[1] Department of Physics and Astronomy, The Johns Hopkins University, Homewood Campus, Baltimore, MD 21218, USA
[2] NASA Goddard Space Flight Centre, Code 662, Greenbelt, MD 20771, USA
[3] Homer L. Dodge Department of Physics and Astronomy, The University of Oklahoma, 440 W. Brooks St., Norman, OK 73019, USA
[4] Department of Physics, Durham University, South Road, Durham DH1 3LE, UK
[5] SUPA, Institute for Astronomy, Royal Observatory of Edinburgh, Blackford Hill, Edinburgh EH9 3HJ, UK
[6] Department of Physics, McGill University, 3600 rue University, Montréal, Québec H3A 2T8, Canada
[7] Chile Observatory, National Astronomical Observatory of Japan, Tokyo 181-8588, Japan
[8] Institute for Computational Cosmology, Durham University, South Road, Durham DH1 3LE, UK
[9] Leiden Observatory, Leiden University, P.O. Box 9513, NL-2300 RA Leiden, The Netherlands

ABSTRACT

We present results from a ≈ 100 ks *Chandra* observation of the 2QZ Cluster 1004+00 structure at $z = 2.23$ (hereafter 2QZ Clus). 2QZ Clus was originally identified as an overdensity of four optically-selected QSOs at $z = 2.23$ within a 15×15 arcmin^2 region. Narrow-band imaging in the near-IR (within the K band) revealed that the structure contains an additional overdensity of 22 $z = 2.23$ Hα-emitting galaxies (HAEs), resulting in 23 unique $z = 2.23$ HAEs/QSOs (22 within the *Chandra* field of view). Our *Chandra* observations reveal that three HAEs in addition to the four QSOs harbor powerfully accreting supermassive black holes (SMBHs), with 2–10 keV luminosities of $\approx (8$–$60) \times 10^{43}$ erg s^{-1} and X-ray spectral slopes consistent with unobscured active galactic nucleus (AGN). Using a large comparison sample of 210 $z = 2.23$ HAEs in the *Chandra*-COSMOS field (C-COSMOS), we find suggestive evidence that the AGN fraction increases with local HAE galaxy density. The 2QZ Clus HAEs reside in a moderately overdense environment (a factor of ≈ 2 times over the field), and after excluding optically-selected QSOs, we find that the AGN fraction is a factor of $\approx 3.5^{+3.8}_{-2.2}$ times higher than C-COSMOS HAEs in similar environments. Using stacking analyses of the *Chandra* data and *Herschel* SPIRE observations at $250\,\mu$m, we respectively estimate mean SMBH accretion rates ($\dot{M}_{\rm BH}$) and star formation rates (SFRs) for the 2QZ Clus and C-COSMOS samples. We find that the mean 2QZ Clus HAE stacked X-ray luminosity is QSO-like ($L_{2-10\,{\rm keV}} \approx [6$–$10] \times 10^{43}$ erg s^{-1}), and the implied $\dot{M}_{\rm BH}/{\rm SFR} \approx (1.6$–$3.2) \times 10^{-3}$ is broadly consistent with the local $M_{\rm BH}/M_{\star}$ relation and $z \approx 2$ X-ray selected AGN. In contrast, the C-COSMOS HAEs are on average an order of magnitude less X-ray luminous and have $\dot{M}_{\rm BH}/{\rm SFR} \approx (0.2$–$0.4) \times 10^{-3}$, somewhat lower than the local $M_{\rm BH}/M_{\star}$ relation, but comparable to that found for $z \approx 1$–2 star-forming galaxies with similar mean X-ray luminosities. We estimate that a periodic QSO phase with duty cycle $\approx 2\%$–8% would be sufficient to bring star-forming galaxies onto the local $M_{\rm BH}/M_{\star}$ relation. This duty cycle is broadly consistent with the observed C-COSMOS HAE AGN fraction ($\approx 0.4\%$–2.3%) for powerful AGN with $L_{\rm X} \gtrsim 10^{44}$ erg s^{-1}. Future observations of 2QZ Clus will be needed to identify key factors responsible for driving the mutual growth of the SMBHs and galaxies.

Key words: cosmology: observations – early universe – galaxies: active – galaxies: clusters: general – surveys – X-rays: general

Online-only material: color figures, machine-readable table

1. INTRODUCTION

Successful theoretical models characterizing the formation and growth history of galaxies and supermassive black holes (SMBHs) generally require that feedback from active galactic nuclei (AGNs) play a crucial role in regulating the growth of galaxy bulges (e.g., De Lucia et al. 2006; Bower et al. 2006, 2008; Croton et al. 2006; Fanidakis et al. 2012), leading to the local M–σ and $M_{\rm BH}$–$M_{\star}$ relations (e.g., Bennert et al. 2011). AGN feedback processes are predicted to be most important in the most massive elliptical galaxies formed within the most massive dark-matter halos. However, in the local universe, these same elliptical galaxies contain the oldest stellar populations and the most dormant SMBHs in terms of their specific mass accretion rates. Mass accretion in these systems is likely limited by the presence of a hot interstellar medium and periodic mechanical feedback from radio powerful AGN (e.g., Best et al. 2005; McNamara & Nulsen 2012). Therefore, directly

observing the growth of these systems requires challenging observations of very distant precursors to today's ellipticals. From models of large-scale structure formation, it is predicted that growth of modern ellipticals takes place in high-density regions at $z \gtrsim 2$–3 (e.g., Kauffmann 1996; Governato et al. 1998; Volonteri et al. 2003; De Lucia et al. 2006).

Thus far, efforts to observe the distant $z \approx 2$–3 galaxy protoclusters SSA22 and HS1700+64, likely pre-cursors to rich local clusters like Coma (e.g., Steidel et al. 1998, 2005), have revealed that the AGN fraction is a factor of ≈ 2–16 times larger (1σ statistical range) in the protocluster environment compared with the low-density field (e.g., Lehmer et al. 2009a, 2009b; Digby-North et al. 2010). This contrasts with local galaxy clusters, which contain lower AGN fractions in their cores (e.g., Martini et al. 2009; Ehlert et al. 2013). The enhanced SMBH growth rate in the protocluster environment is likely linked to the presence of larger gas reservoirs being fed onto more massive galaxies (e.g., Steidel et al. 2005) and SMBHs,

as well as an increase in mergers before the cluster becomes virialized. These structures are therefore ideal for observing and characterizing the interdependent processes involved in the growth of the most massive SMBHs and galaxies, and follow-up studies of protocluster AGN have revealed interesting first results. For example, in the SSA22 protocluster at $z = 3.09$, many of the AGN are found to be coincident with large-scale (~100 kpc) Lyα emitting nebulae (Geach et al. 2009) that may be indicative of emission-line gas being powered by AGN.

To expand upon our efforts to understand AGN activity in the high-density environment at high redshift, we have performed *Chandra* observations of an overdensity of actively star-forming galaxies and optically-selected QSOs at $z = 2.23$: the 2QZ Cluster 1004+00 structure (hereafter 2QZ Clus). 2QZ Clus was discovered by Matsuda et al. (2011) by first searching the 2dF QSO Redshift Survey (2QZ; Croom et al. 2001, 2004) and identifying an overdensity of quasars within the redshift interval $z = 2.216$–2.248, corresponding to the Hα line in the UKIRT WFCAM H$_2$S1 filter, and then performing narrow and broad band near-infrared imaging (via the H$_2$S1 $\lambda_c = 2.121\,\mu$m and K-band filters) to identify star-forming active galaxies at $z = 2.23$ via the Hα emission line. The redshift range of the Hα line corresponding to the 50% transmission wavelengths of the H$_2$S1 band is $z = 2.216$–2.248. These Hα emitters (HAEs) therefore have both redshift identifications and Hα-based measures of their star formation rates (SFRs). Matsuda et al. (2011) revealed that the 2QZ Clus field contains an overdensity of 22 vigorous star-forming HAEs (Hα-based SFR $\gtrsim 14\,M_\odot\,$yr^{-1} without any correction for extinction) in a 13.7×13.7 arcmin^2 region ($\approx 22 \times 22$ comoving Mpc^2). These observations probe the tip of the iceberg of the actively star-forming $z = 2.23$ 2QZ Clus galaxy population with additional contributions from luminous AGN. Identification of the lower-SFR and Hα-obscured population is still needed to fully characterize the large-scale nature of this structure.

In this paper, we present first results from the *Chandra* observations of 2QZ Clus. In Section 2, we discuss our analysis methods and provide reduced data products, including images, exposure maps, and point-source catalogs. In Section 3, we present the properties of the X-ray detected sources in the 2QZ Clus structure, and compare these with an equivalent unbiased sample of $z = 2.23$ HAEs found in the COSMOS survey field from the High-z Emission Line Survey (HiZELS; Geach et al. 2008; Sobral et al. 2009). In Section 4, we compare the relative growth rates of 2QZ Clus SMBHs and galaxies. We further discuss the nature of the 2QZ Clus structure itself and put the AGN activity into the context of the broader $z = 2.23$ population of HAEs found in COSMOS. Finally, in Section 5, we summarize our results.

The Galactic column densities for 2QZ Clus and COSMOS are 3.0×10^{20} cm^{-2} and 2.5×10^{20} cm^{-2}, respectively. All of the X-ray fluxes and luminosities quoted throughout this paper have been corrected for Galactic absorption. In the X-ray band, we make use of three bandpasses: 0.5–2 keV (soft band [SB]), 2–7 keV (hard band [HB]), and 0.5–7 keV (full band [FB]). Values of $H_0 = 70$ km s^{-1} Mpc^{-1}, $\Omega_M = 0.3$, and $\Omega_\Lambda = 0.7$ are adopted throughout this paper (e.g., Spergel et al. 2003).

2. OBSERVATIONS, REDUCTION, AND ANALYSIS

Throughout this paper we will compare the SMBH growth among HAEs in the 2QZ Clus structure with HAEs in the COSMOS field. To do this effectively, we designed our *Chandra* observations of 2QZ Clus to be of comparable depth and quality
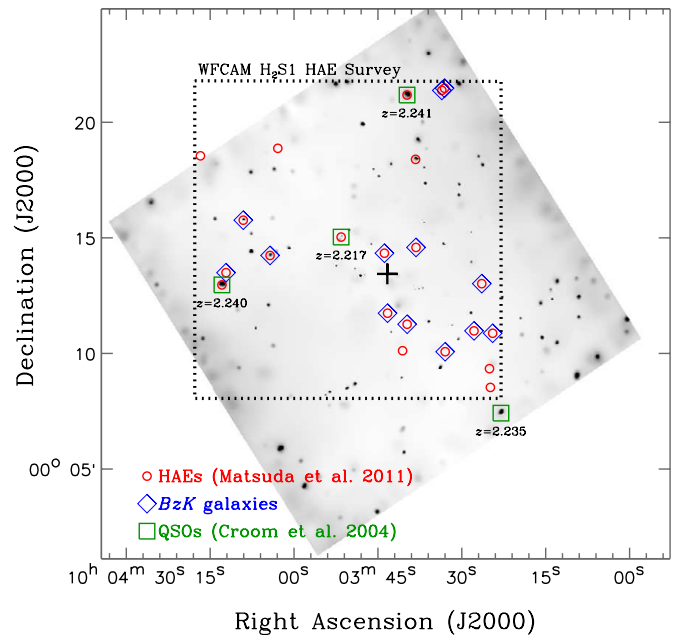
Figure 1. Evidence for wide-spread AGN activity for $z = 2.23$ HAEs in the 2QZ Clus structure. We show the adaptively-smoothed 0.5–7 keV *Chandra* image of the 2QZ Clus field. For illustrative purposes, the image was binned by a factor of four (in both R.A. and decl.) and has been exposure-corrected by dividing the smoothed image by a smoothed exposure map (see Section 2.2). The aim point of the image has been indicated with a cross. The $z = 2.216$–2.248 QSOs that were used to select the 2QZ Clus field have been highlighted with green squares (Croom et al. 2001, 2004). The WFCAM HAE survey region (dashed square) and $z = 2.23$ source candidates (red circles) have been highlighted (see Matsuda et al. 2011). BzK candidates have been highlighted with blue diamonds; these sources have colors consistent with actively star-forming galaxies at $z \approx 1.4$–2.5.

(A color version of this figure is available in the online journal.)

as the *Chandra* data products that are already available from the *Chandra* COSMOS survey (C-COSMOS; Elvis et al. 2009; Puccetti et al. 2009; Civano et al. 2012). Therefore the *Chandra* analysis that follows has been customized to produce catalogs and data products that can be directly compared with those available from C-COSMOS.

2.1. Data Reduction

We obtained a ≈ 100 ks *Chandra* exposure consisting of a single 16.9×16.9 ACIS-I pointing (*Chandra* ObsID 13976; taken over the 2012 January 13 and 14; PI: B. D. Lehmer) centered on the 2QZ Clus region surveyed by Matsuda et al. (2011; see Figure 1).[10] The observation was centered on the aim point coordinates $\alpha_{J2000} = 10{:}03{:}43.3$ and $\delta_{J2000} = +00{:}13{:}26.47$ and was oriented at a roll angle that was 56.9 from north. The total duration of the observation was 99.6 ks. For our data reductions, we made use of CIAO v. 4.4 with CALDB v4.5.0. We began by reprocessing our events lists, bringing level 1 to level 2 using the script chandra_repro. The chandra_repro script runs a variety of CIAO tools that identify and remove events from bad pixels and columns, and filter the events list to include only good time intervals without significant flares and non-cosmic ray events corresponding to the standard *ASCA* grade set (*ASCA* grades 0, 2, 3, 4, 6).

Using the reprocessed level 2 events list, we constructed a first FB image and a point-spread function (PSF) map (using the tool

---

[10] Note that during the observation, the ACIS-S3 chip was on; however, due to its large off-axis angle and non-coincidence with any $z \approx 2.23$ sources in the 2QZ Clus field, we chose to exclude data from the ACIS-S3 CCD.

Table 1
Chandra Point-Source Catalog of the 2QZ Clus Field

Source ID (1)	Position (J2000)		Net Counts			Exposure (ks)			Count-Rate (10^{-4} cnts s^{-1})		
	α_{J2000} (2)	δ_{J2000} (3)	FB (4)–(6)	SB (7)–(9)	HB (10)–(12)	FB (13)	SB (14)	HB (15)	FB (16)–(18)	SB (19)–(21)	HB (22)–(24)
1	10 03 00.7	+00 10 54.1	$16.4^{+10.0}_{-8.9}$	<20.2	<26.0	53.5	47.7	77.2	$2.2^{+2.0}_{-1.8}$	<4.5	<3.7
2	10 03 00.8	+00 11 25.1	$42.2^{+14.2}_{-11.4}$	$21.9^{+10.7}_{-7.7}$	<36.3	24.6	21.9	35.8	$25.0^{+6.1}_{-4.9}$	$13.2^{+5.2}_{-3.7}$	<10.8
3	10 03 05.9	+00 09 49.2	$67.3^{+12.1}_{-11.0}$	<15.5	$66.8^{+11.7}_{-10.6}$	61.7	57.1	80.5	$11.3^{+2.1}_{-1.9}$	<2.8	$8.8^{+1.6}_{-1.4}$
4	10 03 09.2	+00 11 31.1	$24.7^{+8.9}_{-7.7}$	$14.4^{+6.4}_{-5.1}$	<22.4	71.6	68.7	83.3	$3.4^{+1.3}_{-1.1}$	$2.1^{+0.9}_{-0.8}$	<2.8
5	10 03 09.3	+00 12 24.3	$64.2^{+11.3}_{-10.2}$	$27.8^{+7.6}_{-6.4}$	$38.3^{+9.4}_{-8.3}$	69.5	66.1	83.0	$9.2^{+1.7}_{-1.5}$	$4.2^{+1.2}_{-1.0}$	$4.6^{+1.2}_{-1.0}$
6	10 03 09.6	+00 09 01.1	$68.9^{+11.4}_{-10.2}$	$54.5^{+9.5}_{-8.3}$	<21.8	46.0	42.5	60.3	$15.1^{+2.4}_{-2.2}$	$13.2^{+2.2}_{-1.9}$	<3.6
7	10 03 09.8	+00 13 12.9	$14.0^{+8.0}_{-6.8}$	$14.3^{+6.2}_{-5.0}$	<19.7	65.9	61.8	82.6	$2.0^{+1.2}_{-1.0}$	$2.3^{+1.0}_{-0.8}$	<2.4
8	10 03 13.1	+00 13 05.1	$57.7^{+10.2}_{-9.1}$	$29.0^{+7.3}_{-6.1}$	$30.4^{+8.1}_{-6.9}$	74.5	71.9	84.6	$7.9^{+1.4}_{-1.3}$	$4.1^{+1.0}_{-0.9}$	$3.6^{+1.0}_{-0.8}$
9	10 03 13.2	+00 10 26.8	$41.9^{+9.8}_{-8.7}$	$21.6^{+6.9}_{-5.6}$	$20.1^{+7.9}_{-6.7}$	76.3	74.1	85.1	$5.5^{+1.3}_{-1.1}$	$2.9^{+0.9}_{-0.8}$	$2.4^{+0.9}_{-0.8}$
10	10 03 13.9	+00 12 17.5	$13.7^{+7.0}_{-5.7}$	$11.3^{+5.4}_{-4.2}$	<15.6	78.7	77.0	85.9	$1.7^{+0.9}_{-0.8}$	$1.5^{+0.7}_{-0.6}$	<1.9

Notes. Column 1: *Chandra* source ID for 2QZ Clus field. Columns 2 and 3: right ascension (α_{J2000}) and declination (δ_{J2000}), respectively. Right ascension is quoted in units of degrees, minutes, seconds. Declination is quoted in degrees, arcminutes, and arcseconds. Columns 4–12: net counts (N) and 1σ upper/lower bounds, computed following Section 2.2, for FB, SB, and HB. Columns 13–15: vignetting-corrected effective exposure times (in kiloseconds) for FB, SB, and HB, respectively. Columns 16–24: vignetting corrected count-rates and 1σ upper/lower bounds, computed following the methods described in Section 2.2, for FB, SB, and HB. Columns 25–27: X-ray flux in units of erg cm^{-2} s^{-1} for the FB, SB, and HB, respectively. Column 28: notes related to source ("M" = Manual photometry required due to image edge; "H" = Coincident with $z = 2.23$ HAE; "Q" = Coincident with optically identified QSO).

(This table is available in its entirety in a machine-readable form in the online journal. A portion is shown here for guidance regarding its form and content.)

mkpsfmap), which corresponded to a monochromatic energy at 1.497 keV and an encircled counts fraction (ECF) set to 0.393. We constructed an initial source catalog by searching our FB image with wavdetect (run with our PSF map), which was set at a conservative false-positive probability threshold of 1×10^{-7} and run over seven scales from 1–8 (using a $\sqrt{2}$ sequence: 1, $\sqrt{2}$, 2, $2\sqrt{2}$, 4, $4\sqrt{2}$, and 8). To sensitively measure whether any significant flares remained in our observations, we constructed point-source-excluded 0.5–7 keV background light curves for the observation in a variety of time bins (spanning 10–800 s bins). We found no evidence of any significant ($\gtrsim 5\sigma$) flaring events throughout the observation, and therefore considered our reprocessed level 2 events file to be sufficiently cleaned.

Next, using the initial X-ray source catalog and an optical $I < 22$ mag source catalog from the Sloan Digital Sky Survey Data Release 6 (SDSS-DR6; Adelman-McCarthy et al. 2008), we registered our aspect solution and events list to the SDSS-DR6 frame using CIAO tools reproject_aspect and reproject_events, respectively. The resulting astrometric reprojections gave very small astrometric adjustments, including linear translations of $\delta x = -0.12$ pixels and $\delta y = +0.30$ pixels, a rotation of $-0°.0097$, and a pixel scale stretch factor of 1.00018.

2.2. Point-source Catalog Production

Using the reprojected aspect solution and events file (see Section 2.1), we constructed standard-band images, 90% ECF PSF maps (corresponding to 1.497 keV, 4.51 keV, and 2.3 keV for the SB, HB, and FB, respectively), and exposure maps in the three standard bands. The exposure maps were constructed following the basic procedure outlined in Section 3.2 of Hornschemeier et al. (2001); these maps were normalized to the effective exposures of sources located at the aim points. This procedure takes into account the effects of vignetting, gaps between the CCDs, bad column and pixel filtering, and the spatially dependent degradation of the ACIS optical blocking filter. A photon index of $\Gamma = 1.4$ was assumed in creating the expo-

sure maps. In Figure 1, we show the adaptively-smoothed FB image and the locations of HAEs and QSOs that are associated with the 2QZ Clus structure. The image was smoothed using csmooth and was "flattened" by dividing the smoothed image by a smoothed exposure map.

We constructed a *Chandra* source catalog by (1) searching the three standard-band images using wavdetect (including the appropriate 90% ECF PSF and exposure maps) at false-positive probability threshold of 2×10^{-5} (the equivalent detection threshold adopted by Elvis et al. 2009 in the C-COSMOS field); and (2) adjoining the three bandpass catalogs using cross-band matching radii of $2''.5$ and $4''.0$ for sources with off-axis angles of $<6'$ and $>6'$, respectively. Through this procedure, we identified a total of 133 unique X-ray detected sources in the 2QZ Clus field. These 133 sources constitute our main *Chandra* catalog (see Table 1).

We performed aperture photometry for our 133 sources in each of the three standard bands. For each X-ray source, we extracted source plus background counts S_{src} and exposure-map values T_{src} using circular apertures with radii corresponding to the 90% ECF, which were determined using the corresponding PSF-map value at the source location. We visually inspected these regions and found that only two source-pairs had very minor overlaps in the HB PSF (and no overlaps in the smaller SB and FB PSFs). The overlapping regions of these source pairs contained $\leqslant 1$ HB counts; therefore, we did *not* perform any corrections to the photometry for these sources.

For each source, local background counts and exposure values were then extracted from each of the three bandpasses. This was achieved by creating images and exposure maps with all sources masked out of circular masking regions of a radius 1.5 times the size of the 95% encircled energy fraction (estimated using each local PSF). Using these masked data products, we then extracted background counts S_{bkg} and exposure values T_{bkg} from a larger background extraction square aperture that was centered on the source. The size of the background extraction square varied with each source and was chosen to contain $\gtrsim 30$–100 background counts in all bands. For each bandpass, net source counts N were

computed following $N = (S_{src} - S_{bkg} T_{src}/T_{bkg})/\gamma_{ECF}$, where γ_{ECF} is the ECF appropriate for the source extraction region and bandpass. We computed 1σ level Poisson errors on the net counts following the methods described in Gehrels (1986).

To calculate vignetting-corrected count-rates, we made use of count-rate maps, which were constructed by dividing the images by the exposure maps. The advantage of count-rate maps is that they allow for an accurate accounting of the source intensity when gradients in the exposure are present in a source extraction region (e.g., near chip gaps, image edges, and bad pixels). We made use of the same source and background regions described above to extract on-source count-rates ϕ_{src} and background count-rates ϕ_{bkg}. Net count-rates were then computed following $\phi = (\phi_{src} - \phi_{bkg} A_{src}/A_{bkg})/\gamma_{ECF}$, where A_{src} and A_{bkg} are the source and background extraction areas that contain exposure.

For each source, we converted our vignetting-corrected count-rates to fluxes using conversion factors of [1.18, 0.659, and 1.96] $\times 10^{-11}$ erg cm^{-2} s^{-1} (cnts s^{-1})$^{-1}$ for the FB, SB, and HB, respectively. These factors assume a power-law SED with $\Gamma = 1.4$ that is corrected for Galactic extinction. In Table 1, we provide the basic X-ray properties of the 133 main-catalog sources in the 2QZ Clus field. The survey reaches ultimate 5-count sensitivity limits of $\approx 6.0 \times 10^{-16}$ erg cm^{-2} s^{-1}, $\approx 3.4 \times 10^{-16}$ erg cm^{-2} s^{-1}, $\approx 1.0 \times 10^{-15}$ erg cm^{-2} s^{-1} for the FB, SB, and HB, respectively; at $z = 2.23$, these limits allow for the detection of a source with rest-frame 2–10 keV luminosity $L_X \gtrsim 10^{43}$ erg s^{-1}. These limits are nicely compatible with those achieved by the C-COSMOS survey, which reaches a factor of ≈ 1.4–1.7 times deeper in ultimate sensitivity (Elvis et al. 2009).

3. RESULTS

3.1. AGN Activity within $z = 2.23$ 2QZ Clus Structure

To measure the AGN activity in the 2QZ Clus structure at $z = 2.23$, we made use of the catalog of 22 HAEs from Matsuda et al. (2011) and four known $z = 2.23$ QSOs. After accounting for overlap in the HAE/QSO populations, there are a total of 23 unique $z = 2.23$ source candidates (see Figure 1). The one QSO that does not have an HAE counterpart lies outside the footprint of the narrow-band survey and is likely to be an HAE itself based on its selection from optical emission lines. In the HAE survey, Matsuda et al. (2011) selected candidate $z = 2.23$ sources that satisfied the following criteria: (1) $K - H_2S1 \geqslant 0.251$ (EW$_{obs} \geqslant 50$ Å) and (2) the Hα flux excess significance (i.e., the ratio between H$_2$S1 excess and the uncertainty in the $K - H_2S1$ color) $\Sigma \geqslant 2.5$. The narrow-band imaging reaches a H$_2$S1 5σ depth of ≈ 19.9 mag (AB). This selection is inherently subject to minor (at $\lesssim 10\%$–20% level) contamination from Paα emitters at $z = 0.13$, Paβ emitters at $z = 0.65$, and [O III]5007 emitters at $z = 3.24$; however, for many cases we can make use of $B - z'$ and $z' - K$ colors (i.e., the BzK criteria) to constrain the redshifts to $z \sim 1.4$–2.5 and rule-out such contaminants. The BzK criteria includes $(z' - K)_{AB} - (B - z')_{AB} \geqslant -0.2$ or $(z' - K)_{AB} > 2.5$ (Daddi et al. 2004). From Matsuda et al. (2011), 17 out of the 23 $z = 2.23$ are either spectroscopically confirmed 2QZ Clus structure member QSOs or satisfy the BzK criteria (see Figure 1). Interestingly, the three QSOs with B, z, K photometry do not satisfy the BzK selection criteria, indicating that AGN-dominated SEDs can be missed by these criteria. This is likely due to the presence of strong emission lines, and indeed the three QSOs lie only ≈ 0.1–0.2 mag away from the BzK selection line (see Figure 3 of Matsuda et al. 2011).
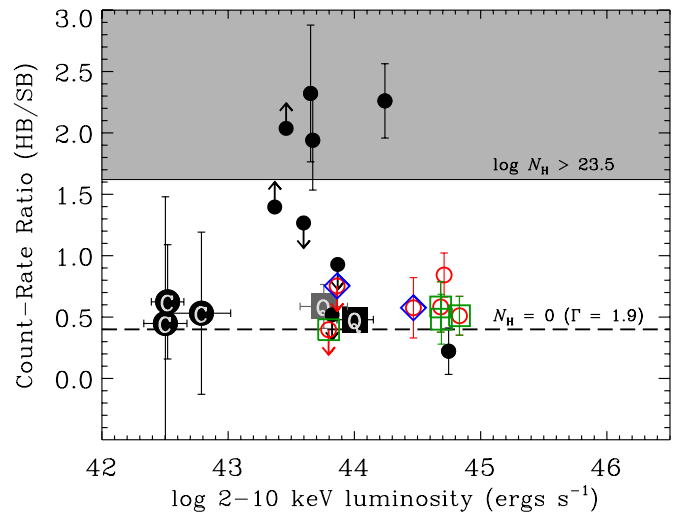
Figure 2. Observed X-ray spectral shapes (HB-to-SB count-rate ratio) vs. 2–10 keV luminosity for X-ray detected $z = 2.23$ HAEs and QSOs in 2QZ Clus and C-COSMOS fields. The red open circles and green open squares show 2QZ Clus HAEs and $z = 2.23$ QSOs, respectively; blue diamonds indicate sources that satisfy the BzK star-forming galaxy criteria. C-COSMOS $z = 2.23$ HAEs are shown as filled circles. The results from stacking HAE samples in different overdensity bins in C-COSMOS are shown as black circles with the letter "C" and stacking of 2QZ Clus HAE samples including and excluding pre-selected QSOs used to identify the 2QZ Clus structure are respectively shown as black and gray squares with the letter "Q" (see Section 4.2 for details). The horizontal dashed line shows the expected count-rate ratio for an unobscured AGN with a power-law SED of $\Gamma = 1.9$. The shaded region shows the expected count-rate ratio for AGN obscured by a column of log(N_H/cm^{-2}) $\gtrsim 23.5$. All of the 2QZ Clus sources have spectral shapes consistent with luminous unobscured AGN, while the C-COSMOS AGN span a broader range of spectral slopes.

(A color version of this figure is available in the online journal.)

One HAE of the 23 $z = 2.23$ sources is located outside of the *Chandra* field of view. We matched the remaining 22 sources (21 HAEs and four $z = 2.23$ QSOs) to our 2QZ Clus *Chandra* catalog using a 2″.5 matching radius (see annotations in Figure 1). Given the HAE and X-ray source densities, we estimate that this choice of matching radius will lead to a negligible number of random associations (i.e., a total of ≈ 0.02 false-matches expected). We find a total of seven matches, giving an initial AGN fraction of $\approx 32^{+17}_{-12}\%$ (1σ intervals based on Gehrels 1986). Four of the seven X-ray detected sources are the optically-identified QSOs that were used to originally select the 2QZ Clus for study (see Matsuda et al. 2011 for details); therefore, three additional $z = 2.23$ AGN are identified here as a result of our *Chandra* observations. If we exclude the four pre-selected QSOs, the AGN fraction of the underlying HAE population is $\approx 17^{+16}_{-9}\%$. Six of the seven X-ray detected sources are either spectroscopically confirmed 2QZ Clus member QSOs or BzK galaxies and are unlikely to be interlopers. The one HAE (XID = 49) that does not satisfy either criteria is inferred to be very luminous log L_X/erg s$^{-1} \approx 44.7$ and may have an AGN-dominated SED that does not satisfy the BzK criteria (similar to the other known QSOs); however, we cannot rule out the possibility that this source is a low-redshift interloper. In Figure 2, we show the HB-to-SB count-rate ratio versus 2–10 keV luminosity for X-ray-detected HAEs and $z = 2.23$ QSOs in the 2QZ Clus field, and in Table 2, we list the properties of these sources. These seven X-ray sources have HB-to-SB count-rate ratios and X-ray luminosities that are consistent with powerful unobscured QSOs.

In Figure 3, we show the distributions of Hα fluxes for the 2QZ Clus HAEs and highlight the subset of HAEs with X-ray

Table 2
X-Ray Detected HAEs and QSOs in the 2QZ Clus and C-COSMOS Fields

α_{J2000} (1)	δ_{J2000} (2)	XID (3)	SB (4)	HB (5)	$\phi_{2-7\,keV}/\phi_{0.5-2\,keV}$ (6)	$\log f_{0.5-7\,keV}$ (erg cm^{-2} s^{-1}) (7)	$\log L_X$ (erg s^{-1}) (8)	$\log f_{H\alpha}$ (erg cm^{-2} s^{-1}) (9)	$\log L_{H\alpha}$ (erg s^{-1}) (10)	Notes (11)
2QZ Clus
10 03 23.0	+00 07 25.0	17	15.1 ± 1.8	7.3 ± 1.2	0.48 ± 0.20	-13.6	44.7	$\cdots$	$\cdots$	QSO
10 03 38.3	+00 18 23.8	49	13.0 ± 1.6	10.9 ± 1.5	0.84 ± 0.18	-13.5	44.7	-15.3	43.3	
10 03 39.8	+00 21 10.8	58	14.6 ± 1.8	8.5 ± 1.4	0.58 ± 0.21	-13.6	44.7	-14.8	43.7	QSO
10 03 51.6	+00 15 02.1	96	3.0 ± 1.1	<1.2	>0.40	-14.5	43.8	-15.2	43.4	QSO
10 04 04.3	+00 14 14.4	118	8.7 ± 1.3	5.0 ± 1.0	0.58 ± 0.25	-13.8	44.5	-16.3	42.3	*BzK*
10 04 09.1	+00 15 45.9	126	2.7 ± 0.8	<2.0	>0.75	-14.4	43.9	-16.2	42.3	*BzK*
10 04 12.9	+00 12 57.9	129	21.3 ± 1.9	10.9 ± 1.4	0.51 ± 0.16	-13.4	44.8	-14.7	43.9	QSO
C-COSMOS
09 58 54.6	+02 14 03.6	864	2.3 ± 0.6	5.2 ± 0.9	2.26 ± 0.30	-14.0	44.2	-16.2	42.4	
10 00 02.6	+02 19 58.7	774	0.7 ± 0.2	1.3 ± 0.3	1.94 ± 0.41	-14.6	43.7	-15.6	43.0	*BzK*
10 00 26.6	+01 58 23.0	716	0.6 ± 0.3	1.3 ± 0.4	2.32 ± 0.56	-14.6	43.7	-15.9	42.7	*BzK*
10 00 44.2	+02 02 06.9	1456	<0.5	1.1 ± 0.3	<2.04	-14.8	43.5	-16.0	42.6	*BzK*
10 00 55.4	+01 59 55.4	1486	<0.6	0.8 ± 0.3	<1.40	-14.9	43.4	-16.1	42.5	*BzK*
10 00 55.4	+02 33 30.1	1386	2.8 ± 0.6	<2.6	>0.93	-14.4	43.9	-15.8	42.8	
10 00 57.5	+02 33 45.2	929	2.7 ± 0.6	<1.4	>0.52	-14.4	43.8	-15.7	42.9	
10 01 15.2	+01 57 13.3	1105	1.5 ± 0.3	<1.9	>1.27	-14.7	43.6	-16.2	42.4	*BzK*
10 01 29.9	+02 17 04.1	1261	0.5 ± 0.2	<1.7	>3.21	-15.1	43.2	-15.1	43.5	
10 01 53.5	+02 11 51.6	451	18.0 ± 1.4	4.0 ± 0.7	0.22 ± 0.19	-13.5	44.7	-16.0	42.6	

Notes. Columns 1 and 2: optical/near-IR right ascension (α_{J2000}) and declination (δ_{J2000}), respectively. Right ascension is quoted in units of degrees, minutes, seconds. Declination is quoted in degrees, arcminutes, and arcseconds. Column 3: X-ray catalog ID (XID). For sources in the 2QZ Clus field, the XID is from this work (see Table 1), and for the C-COSMOS sources, the XID is from Elvis et al. (2009). Columns 4 and 5: count-rate for the SB and HB, respectively, in units of 10^{-4} cnts s^{-1}. Column 6: count-rate ratio between the 2–7 keV and 0.5–2 keV bands. Column 7: logarithm of the 0.5–7 keV source flux in erg cm^{-2} s^{-1}. Column 8: logarithm of the rest-frame 2–10 keV luminosity in units of erg s^{-1}. Luminosities were calculated assuming each source is at $z = 2.23$. Columns 9 and 10: logarithm of the Hα source flux (in erg cm^{-2} s^{-1}) and luminosity (in erg s^{-1}), respectively, as provided by Matsuda et al. (2011) for the 2QZ Clus field and Sobral et al. (2013) for the C-COSMOS field. Column 11: notes on X-ray detected sources.

detections. We find that the AGN occupy the bright-end of the Hα flux distribution ($f_{H\alpha} \gtrsim 2 \times 10^{-16}$ erg cm^{-2} s^{-1}), indicating (not surprisingly) that the AGN themselves have a dominant contribution to the intensity of the Hα emission lines in these systems. The mean Hα flux of the 2QZ Clus sample overall appears to be higher than any of the non-AGN HAEs, indicating that the bulk of the Hα power from the 2QZ Clus population is likely to be from AGN. However, once the pre-selected QSOs are removed, the mean Hα flux of the 2QZ Clus sample is within the range of the star-forming galaxies. A K-S test reveals that both the 2QZ Clus and C-COSMOS Hα flux distributions are consistent with each other whether or not pre-selected QSOs are included.

3.2. Comparison with C-COSMOS

One of our key goals is to compare the AGN activity of $z = 2.23$ HAEs in the 2QZ Clus structure with that of HAE field samples. As described in Section 1, the 2QZ Clus structure was initially selected as an overdensity of QSOs, and therefore represents a region biased toward both active SMBH mass accretion and galaxy stellar growth. To put into broader context the AGN activity in the 2QZ Clus structure, we make use of an independent sample of $z = 2.216$–2.248 HAEs from HiZELS in the wide-area ≈ 1.6 deg^2 COSMOS survey field (Sobral et al. 2013; see also Geach et al. 2012). The HiZELS HAEs were selected using the same telescopes, cameras, and filters as used for the 2QZ Clus HAE selection; however, unlike 2QZ Clus, the COSMOS field was not selected to have any QSO

overdensity at $z = 2.23$. In total there are 353 $z = 2.23$ HAE candidates with $f_{H\alpha} \gtrsim 5 \times 10^{-17}$ erg cm^{-2} s^{-1} (complete at the $\approx 90\%$ level) that satisfy the criteria used to select the 2QZ Clus HAEs (i.e., $K-H_2S1 \geqslant 0.215$; $H_2S1 \leqslant 19.9$ mag). In this selection, we do not remove non-BzK galaxies for fair comparisons with 2QZ Clus HAEs and to avoid $z = 2.23$ AGN being removed (see discussion in Section 3.1 regarding $z = 2.23$ 2QZ Clus QSOs that do not satisfy BzK selection). As such, our selection is somewhat more liberal than the final selection of galaxies presented in Sobral et al. (2013), which do include a BzK filtering (slightly modified), together with another color–color selection (UBR), high quality photometric redshifts, and information on double/triple line emitters (see Sobral et al. 2013 for details).

Of the 353 HiZELS HAEs, 210 overlap with the footprint of the *Chandra*-COSMOS survey (C-COSMOS; Elvis et al. 2009; Puccetti et al. 2009). C-COSMOS is a contiguous ≈ 0.92 deg^2 *Chandra* survey that reaches 70–180 ks depths (vignetting-corrected) across $\approx 84\%$ of the surveyed area. The combination of the HiZELS HAE and C-COSMOS surveys therefore constitutes a powerful data set by which direct comparisons can be made with the 2QZ Clus data. We made use of the BzK technique to make a first-order assessment of the contamination fraction for our HAE sample. Of these 210 HAEs, we found that 160 had B, z, and K photometry that would allow for a BzK redshift assessment. Of these 160 HAEs, 132 ($\approx 83\%$) have colors satisfying the BzK color selection. We note that this BzK fraction is larger than that reported by Sobral et al. (2013) for the full HAE sample. The difference here is that we have limited
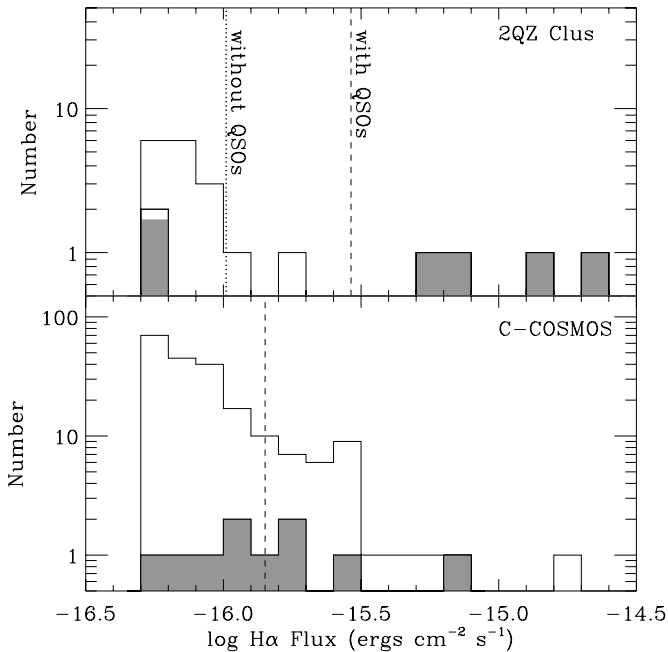
Figure 3. Hα flux distributions of $z = 2.23$ HAEs (open histograms) and their AGN subpopulations (filled histograms) for the 2QZ Clus (top) and C-COSMOS (bottom) samples. The AGN population appears to be preferentially located in HAEs with high Hα flux, indicating that the HAE flux itself is likely influenced by the AGN. The vertical dashed line in each panel shows the mean Hα flux of each sample. We note that the mean Hα flux of 2QZ Clus including pre-selected QSOs appears to be higher than any non-AGN HAEs, suggesting that the selection of this sample is overwhelmed by the AGN. When we exclude pre-selected QSOs, the mean Hα flux becomes more consistent with that of the C-COSMOS field and the star-forming galaxy population (vertical dotted line).

our analysis to the relatively bright HAEs in the HiZELS sample, which has a lower contamination fraction. Furthermore, the BzK fraction for our HAEs is consistent with that found for the 2QZ Clus HAE sample. We have tested the effects of excluding all non-BzK HAEs from our samples and find that this choice has an insignificant impact on the results presented throughout this paper.

Using a matching radius of $2''.5$, we obtain a total of 10 *Chandra* sources matched to the 210 HiZELS HAEs that were within the C-COSMOS footprint, giving an initial AGN fraction of $4.8^{+2.0}_{-1.4}\%$; a factor of $6.7^{+4.7}_{-3.2}$ times lower than the initial 2QZ Clus AGN fraction of $32^{+17}_{-12}\%$. Given the QSO pre-selection in the 2QZ Clus field, this difference in AGN fraction may not be so surprising. When we exclude the four pre-selected QSOs from our computation, we find the 2QZ Clus AGN fraction is $\approx 17^{+16}_{-9}\%$ (i.e., 3 AGN out of 18 HAEs); still a factor of $3.5^{+3.8}_{-2.2}$ times higher than the HiZELS AGN fraction. If we assume that the C-COSMOS HAE AGN fraction is representative of the HAE population in general, we estimate that the binomial probability of detecting 3 or more AGN out of 18 HAEs is $\approx 6\%$.

In Figure 2, we show the count-rate ratio versus 2–10 keV luminosity for the HiZELS $z = 2.23$ HAEs that are X-ray detected in C-COSMOS. The HiZELS HAEs host an almost equal blend of moderately obscured ($N_H \gtrsim 10^{22}$ cm^2) and unobscured AGN as measured by their band ratios. This appears to differ somewhat from the "softer" AGN found in 2QZ Clus (see Figure 2). If we assume that the $\approx 50\%$ ratio of obscured to unobscured AGN in the C-COSMOS HAEs is typical of $z = 2.23$ HAEs, then the probability of finding all three uniquely

X-ray selected AGN (i.e., excluding the four pre-selected QSOs) in 2QZ Clus to be unobscured is $\approx 25\%$. We therefore do not conclude that the differences between the X-ray spectral slopes in 2QZ Clus HAEs are significantly different from those of C-COSMOS HAEs. In Figure 3, we display the Hα flux distribution of the C-COSMOS HAEs and highlight the subset that are X-ray AGN. In contrast to 2QZ Clus HAEs, we find that the mean C-COSMOS HAE flux is within the distribution of non-AGN HAEs, indicating that the total Hα power output is likely dominated by the star-forming galaxy population.

4. DISCUSSION

The above analyses indicate that the 2QZ Clus HAEs contain an enhanced AGN fraction compared to HAEs found in the C-COSMOS field. Here we discuss the possible circumstances surrounding the enhanced SMBH growth in the 2QZ Clus structure. We further put into context the mutual SMBH and galaxy growth of 2QZ Clus and C-COSMOS HAEs.

4.1. Environment as a Driver of Galaxy and SMBH Growth

To assess the role that environment plays in driving SMBH accretion in the HAE population, we made use of the wide-area HiZELS HAEs in the C-COSMOS survey to estimate AGN fraction as a function of source density. For the broader HiZELS HAE sample (i.e., the ≈ 1.6 deg^2 sample), we measured local HAE overdensities for each source following $\rho/\langle\rho\rangle \approx 4/(\pi r_4^2)/\langle\rho\rangle$, where r_4 is the separation between a given source and its fourth nearest neighbor and $\langle\rho\rangle$ is the mean HAE source density over the entire HiZELS COSMOS field. Since the HiZELS COSMOS field has wider aerial coverage than the subpopulation of HAEs that lie within the C-COSMOS footprint, we expect that $\rho/\langle\rho\rangle$ should provide a good estimate of the local source environment for all C-COSMOS sources without suffering from uncertainties due to survey edge effects. Focusing on only the HAEs that were within the C-COSMOS footprint, we divided the sample into three bins of source overdensity, $\log \rho/\langle\rho\rangle = [-0.35, 0.35, 1.12] \pm 0.38$. For each bin, we computed the fraction of HAEs hosting luminous AGN detected in the X-ray band. Figure 4(a) shows the AGN fraction as a function of overdensity $\rho/\langle\rho\rangle$ for the C-COSMOS sources, and in Table 3 we tabulate the AGN fractions of each subset. We find suggestive evidence for an increase in AGN fraction with local HAE source density, such that the $f_{AGN}(\log \rho/\langle\rho\rangle \approx 1.12) = 3.4^{+7.0}_{-2.7} \times f_{AGN}(\log \rho/\langle\rho\rangle \approx -0.4)$. A similar trend was noted for Lyα emitters in the $z = 3.1$ SSA22 protocluster (Lehmer et al. 2009a).

Given that the 2QZ Clus HAE survey is somewhat shallower and less complete than the HiZELS COSMOS HAE survey, we cannot directly compute the equivalent HAE source density all the way down to the Hα flux limit. Therefore, to estimate an average $\rho/\langle\rho\rangle$ for all sources in 2QZ Clus, we computed the survey-wide 2QZ Clus HAE source density of a highly complete ($\gtrsim 90\%$) subsample using only relatively bright HAEs ($f_{H\alpha} > 6.3 \times 10^{-17}$ erg cm^{-2} s^{-1}), and then compared this with the source density of relatively bright COSMOS HiZELS HAEs. The relative bright-source densities indicate that the 2QZ Clus HAEs have on average $\langle\rho\rangle^{bright}_{2QZClus}/\langle\rho\rangle^{bright}_{HiZELS} = 2.0 \pm 0.5$. This value is somewhat higher than, although consistent with, the $\approx 1.5 \pm 0.4$ value found by Matsuda et al. (2011) when comparing the 2QZ Clus HAEs with a smaller HAE control sample. We note that the relatively small area in 2QZ Clus limits us from effectively measuring the local densities of each
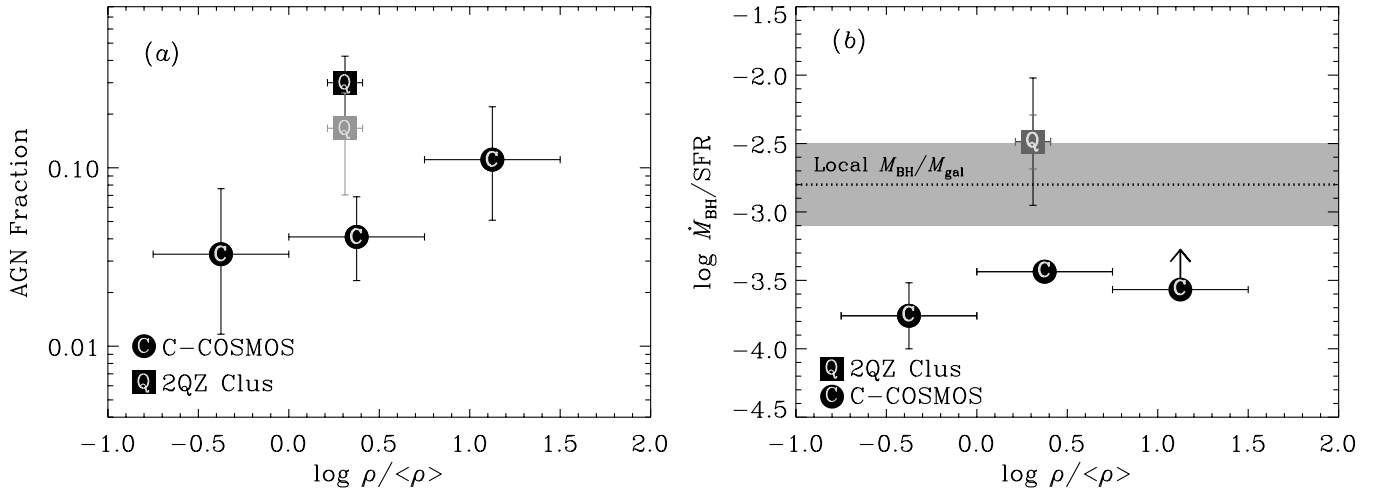
Figure 4. (a) AGN fraction vs. local source overdensity for the C-COSMOS (filled circles) and 2QZ Clus (filled squares) $z = 2.23$ HAEs. For the 2QZ Clus field, we have highlighted results for both the inclusion (black squares) and exclusion (gray squares) of the QSOs that were identified via the 2dF QSO Redshift Survey and used to select the 2QZ Clus field. We find suggestive evidence for an increase in AGN fraction with local density for the C-COSMOS HAEs and find that the 2QZ Clus AGN fraction is significantly elevated over that of the C-COSMOS HAEs. (b) Mean SMBH mass accretion rate per SFR vs. local overdensity for each of the stacked samples presented in Section 4.2 and Table 3. For comparison, the local M_{BH}/M_{gal} relation and its dispersion from Häring & Rix (2004) has been shown as a dotted line with shaded region. The $\dot{M}_{BH}/SFR$ values for 2QZ Clus HAEs appear to be consistent with the local M_{BH}/M_{gal} relation, while the C-COSMOS HAEs fall below this relation. We are unable to determine whether $\dot{M}_{BH}/SFR$ varies with local environment for the C-COSMOS HAEs.

Table 3
X-Ray Stacking of HAE Samples

Sample (1)	$\log(\rho/\langle\rho\rangle)$ (2)	N_{gal} (3)	N_{AGN} (4)	f_{AGN} (5)	$\phi_{2-7\,keV}/\phi_{0.5-2\,keV}$ (6)	$\log L_X$ (erg s^{-1}) (7)	$\dot{M}_{BH}$ ($10^{-3}\,M_\odot$ yr^{-1}) (8)	$S_{250\,\mu m}$ (mJy) (9)	SFR ($M_\odot$ yr^{-1}) (10)
C-COSMOS low density	-0.38 ± 0.38	61	2	$0.03^{+0.04}_{-0.02}$	0.62 ± 0.47	42.52 ± 0.13	11 ± 4	3.9 ± 1.6	68 ± 29
Medium density	0.38 ± 0.38	122	5	$0.04^{+0.03}_{-0.02}$	0.53 ± 0.66	42.79 ± 0.23	21 ± 15	3.4 ± 0.6	60 ± 10
High density	1.12 ± 0.38	27	3	$0.11^{+0.11}_{-0.06}$	0.45 ± 1.03	42.50 ± 0.17	11 ± 5	<2.3	<42
2QZ Clus including QSOs	0.31 ± 0.10	21	6	$0.29^{+0.17}_{-0.11}$	0.48 ± 0.10	44.01 ± 0.14	362 ± 142	6.0 ± 2.6	111 ± 73
Excluding QSOs	0.31 ± 0.10	18	3	$0.17^{+0.16}_{-0.09}$	0.59 ± 0.18	43.76 ± 0.19	204 ± 110	3.6 ± 1.3	63 ± 23

Notes. Column 1: description of $z = 2.23$ HAE sample being stacked. Column 2: HAE source overdensity, $\rho/\langle\rho\rangle$, computed as the ratio of the local HAE source density ρ to mean HAE density across the entire HiZELS COSMOS survey area $\langle\rho\rangle$ (Sobral et al. 2013). For the shallower 2QZ Clus HAE sample, we computed $\rho/\langle\rho\rangle$ using bright HAEs in both the 2QZ Clus and HiZELS COSMOS fields (see Section 4 for details). Column 3: number of galaxies in the relevant stacking sample. This number reflects the exclusion of HAEs that were outside the C-COSMOS footprint, as well as sources that were in the near vicinity (within $\approx 15''$) of unrelated X-ray detected sources. Column 4: number of sources that were detected in the X-ray band. Due to the relatively high survey luminosity limits for $z = 2.23$, these sources are expected to be AGN. Column 5: AGN fraction of sample. Column 6: ratio of stacked 2–7 keV to 0.5–2 keV count-rates ϕ. Column 7: logarithm of the mean 2–10 keV luminosity calculated using the stacked 0.5–2 keV emission. Column 8: estimate of the mean BH accretion rate based on the X-ray luminosity (see Section 4 for details and assumptions). Column 9: mean 250 μm flux in mJy based on stacking analyses. Column 10: mean SFR based on 250 μm flux (see Section 4.2).

galaxy in the way we did for the HiZELS HAEs. A wider area HAE survey of the 2QZ Clus structure would mitigate this limitation. In Figure 4(a), we highlight the AGN fraction of the 2QZ Clus HAEs, both including and excluding HAEs that were pre-selected to be QSOs. After excluding the pre-selected QSOs, we find that the 2QZ Clus AGN fraction is a factor of $\approx 4.1^{+5.0}_{-2.8}$ times higher than the AGN fraction of C-COSMOS HAEs in similarly overdense environments.

From the above analyses, it appears as though the enhanced AGN fraction in the 2QZ Clus cannot be explained by an enhanced source density. However, given that the HAE source selection is limited to the detection of sources with high SFR (SFR $\gtrsim 14\,M_\odot$ yr^{-1}) or AGN activity, it may be possible that there are large numbers of 2QZ Clus galaxies that are lower SFR and/or high Hα extinction leading to an inaccurate characterization of the local source environment. For this to explain the relatively large AGN fraction in terms of environment would require that the underlying galaxy population in 2QZ Clus be very

different from that of C-COSMOS. Future observations sensitive to these galaxy populations would be needed to address this.

If we assume that the enhanced AGN fraction in the 2QZ Clus structure is due solely to the biased QSO-based selection and that our estimates of the local source overdensities are representative of the true environments in which the galaxies are found, we can assess how rarely we should find such elevated AGN fractions. From our analysis of the C-COSMOS HAEs, we know that the probability of an HAE hosting an AGN in an environment like that of 2QZ Clus is $\approx 4\%$. Assuming this incidence fraction is representative of the broader HAE population, we used the binomial probability distribution to compute the rarity of finding AGN fraction enhancements like those of 2QZ Clus. We find that the probability of detecting 3 or more AGN in 18 HAEs (i.e., after removing pre-selected QSOs) is $\approx 4.1\%$. This suggests that there is likely to be something inherently "special" about the 2QZ Clus region; perhaps some unaccounted for physical mechanism is responsible for the enhanced AGN activity that

is unique to 2QZ Clus. It is also possible that the elevated AGN fraction is a product of the presence of more massive host galaxies and SMBHs. For example, Xue et al. (2010) found that the AGN fraction increases rapidly with stellar mass. From their AGN fraction versus stellar mass relations for luminous AGN (see Figure 14(B) of Xue et al. 2010), we infer that the 2QZ Clus galaxies would have to be on-average a factor of ≈5–8 times more massive than the C-COSMOS galaxy population to explain the enhanced AGN fraction that is observed. The 2QZ Clus and C-COSMOS HAEs were selected at the same SFR limits and have similar mean SFRs (see below). Since SFR is in general correlated with stellar mass, with a dispersion of a factor of ≈2 (e.g., Elbaz et al. 2007; Salim et al. 2007), it is unlikely that the mean stellar masses of the HAEs in 2QZ Clus would be ≈5–8 times higher on-average than those in C-COSMOS. Better characterization of the 2QZ Clus HAE source properties, large-scale environment, and underlying non-HAE galaxy population will help us understand this. This could be achieved via *HST* WFC3 infrared observations of the HAE population and/or spectroscopic follow-up of BX/BM and *BzK* galaxy candidates.

4.2. Relative SMBH and Galaxy Growth Rates

To estimate the mean SMBH growth rates of 2QZ Clus and C-COSMOS HAEs, we performed X-ray stacking following the techniques described in Lehmer et al. (2008), with errors measured as 1σ intervals of bootstrap resampling (see, e.g., Basu-Zych et al. 2013 for details). In 2QZ Clus, we stacked the total HAE samples both including and excluding the pre-selected QSOs. For C-COSMOS, we stacked each of the three subsamples that were divided based on source density (see Section 4.1). In Table 3, we tabulate our stacking results for the five subsamples. We find that the stacked 2–10 keV luminosities range from $\log L_X/(\text{erg s}^{-1}) \approx 42.5$–44, indicating that AGN clearly dominate the mean stacked X-ray emission over normal galaxy emission by more than an order of magnitude for galaxies of similar SFRs and redshifts (e.g., Lehmer et al. 2010; Basu-Zych et al. 2013). In all cases the 2–7 keV/0.5–2 keV count-rate ratios indicate the mean stacked spectrum is consistent with unobscured AGN (see Figure 2 and Column 6 in Table 3). We converted our mean 2–10 keV luminosities into bolometric luminosities $L_{\text{bol}}^{\text{AGN}}$ using a correction factor of 22.4, which corresponds to the median bolometric correction for local AGN with $L_X \approx 10^{41}$–10^{46} erg s^{-1} (Vasudevan & Fabian 2007). We then estimated the mean SMBH accretion rates following $\dot{M}_{\text{BH}} \approx (1 - \epsilon)L_{\text{bol}}^{\text{AGN}}/(\epsilon c^2)$, where c is the speed of light and ϵ is the efficiency by which accreting mass is converted into radiative energy; here we assume $\epsilon \approx 0.1$ (see, e.g., Marconi et al. 2004 for motivation). These assumptions yield mean mass accretion rates spanning $\dot{M}_{\text{BH}} \approx 0.01$–$0.02 \, M_\odot$ yr^{-1} for the C-COSMOS HAE samples and ≈0.2–0.4 $M_\odot$ yr^{-1} for the 2QZ Clus HAE samples (see Column 8 in Table 3).

The above X-ray stacking shows that the mean SMBH accretion rates of 2QZ Clus HAEs are significantly larger than those of C-COSMOS HAEs; however, we want to test whether the corresponding SFRs of the HAEs are on average consistent with that expected from the local $M_{\text{BH}}/M_{\text{gal}}$ relation. Although the Hα emission line provides an immediate proxy for the SFR, Hα is often subject to extinction in starburst galaxies like those studied here (e.g., Calzetti 1997). Furthermore, in the case of QSOs, the Hα emission line fluxes from the AGN will overwhelm any signal related to star formation activity, making

it difficult to infer directly the SFRs of these sources (see, e.g., Figure 3).

To remedy these issues, we have made use of *Herschel* observations at 250 μm using the Spectral and Photometric Imaging Receiver (SPIRE). *Herschel* SPIRE data are available in the C-COSMOS field via the HerMES campaign (Oliver et al. 2012) and in the 2QZ Clus field through a GO program (PI: Matsuda; Y. Matsuda et al. 2013, in preparation). These data allow us to probe emission from the rest-frame 80 μm, which is well beyond the peak of the expected dust-emission associated with QSOs (≈6–15 μm; e.g., Efstathiou & Rowan-Robinson 1995; Netzer et al. 2007; Hatziminaoglou et al. 2010; Mullaney et al. 2011). We therefore anticipate that SPIRE probes the cool dust emission associated with star formation activity, and the total SFR can be measured using these data. We performed SPIRE stacking of the three C-COSMOS and two 2QZ Clus samples described in Table 3 following the techniques detailed in Harrison et al. (2012). We obtained significant signal in the 250 μm stacks for all samples except for the highest overdensity C-COSMOS subsample (see Table 3). Errors on mean SPIRE flux represent the largest 1σ interval based on bootstrap resampling (see Harrison et al. 2012 for details). We converted 250 μm fluxes to L_{IR} (8–1000 μm) using the SED library of Chary & Elbaz (2001), selecting a SED (redshifted to $z = 2.23$) on the basis of the total monochromatic luminosity probed by the 250 μm emission. We converted the infrared luminosities to SFRs following SFR$/(M_\odot$ yr$^{-1}) \approx 9.8 \times 10^{-11} \times L_{\text{IR}}/L_\odot$. This conversion assumes negligible contributions from UV emission and is appropriate for a Kroupa (2001) initial mass function (IMF; see Equation (1) of Bell et al. 2005). The mean SFRs are reported in Column 10 of Table 3.

From the above X-ray and infrared stacking analyses, we obtain mean $\dot{M}_{\text{BH}}$/SFR ratios for our samples. In Figure 4(b), we display $\dot{M}_{\text{BH}}$/SFR versus overdensity ($\rho/\langle\rho\rangle$) for these samples. We find that the 2QZ Clus HAEs have $\dot{M}_{\text{BH}}$/SFR $\approx 3.2 \times 10^{-3}$, similar to the mean $M_{\text{BH}}/M_{\text{gal}}$ ratio at $z = 0$ (e.g., Häring & Rix 2004; Bennert et al. 2011). For the C-COSMOS HAE subsamples, we find much lower values of $\dot{M}_{\text{BH}}$/SFR $\approx (0.2$–$0.4) \times 10^{-3}$. Such a deficit in SMBH-to-galaxy growth rate ratio may be due to the SFR-biased selection of C-COSMOS HAEs, which has constrained our analysis to include only powerful star-forming galaxies with extinction uncorrected Hα-based SFR$_{\text{H}\alpha} > 14 \, M_\odot$ yr^{-1}.

Recent *Herschel* SPIRE analyses of X-ray selected AGN in the CDF-N, CDF-S, and COSMOS fields have shown that on average the mean SFR increases with mean AGN luminosity; however, there is some debate as to whether the most powerful QSOs with $L_X \gtrsim 10^{44}$ erg s^{-1} have declining SFRs (e.g., Harrison et al. 2012; Page et al. 2012). In the left panel of Figure 5, we compare the 2QZ Clus and C-COSMOS HAE $\dot{M}_{\text{BH}}$/SFR values with those of X-ray selected AGN presented in Harrison et al. (2012) and $z \approx 1$–3 AGN from Mullaney et al. (2012b). X-ray luminosities have been converted to $\dot{M}_{\text{BH}}$ following the techniques discussed above and SFRs have been converted to be consistent with our choice of Kroupa (2001) IMF. It is apparent that the mean $\dot{M}_{\text{BH}}$/SFR for X-ray selected AGN appears to be consistent with the local $M_{\text{BH}}/M_{\text{gal}}$ relation (Häring & Rix 2004) for AGN with $L_X \lesssim 10^{44}$ erg s^{-1}. At higher L_X, $M_{\text{BH}}/M_{\text{gal}}$ increases dramatically. The 2QZ Clus HAE samples have $\dot{M}_{\text{BH}}$/SFR versus L_X mean values in good agreement with the trends observed for the Harrison et al. (2012) X-ray selected AGN (see Figure 5). As discussed above, the
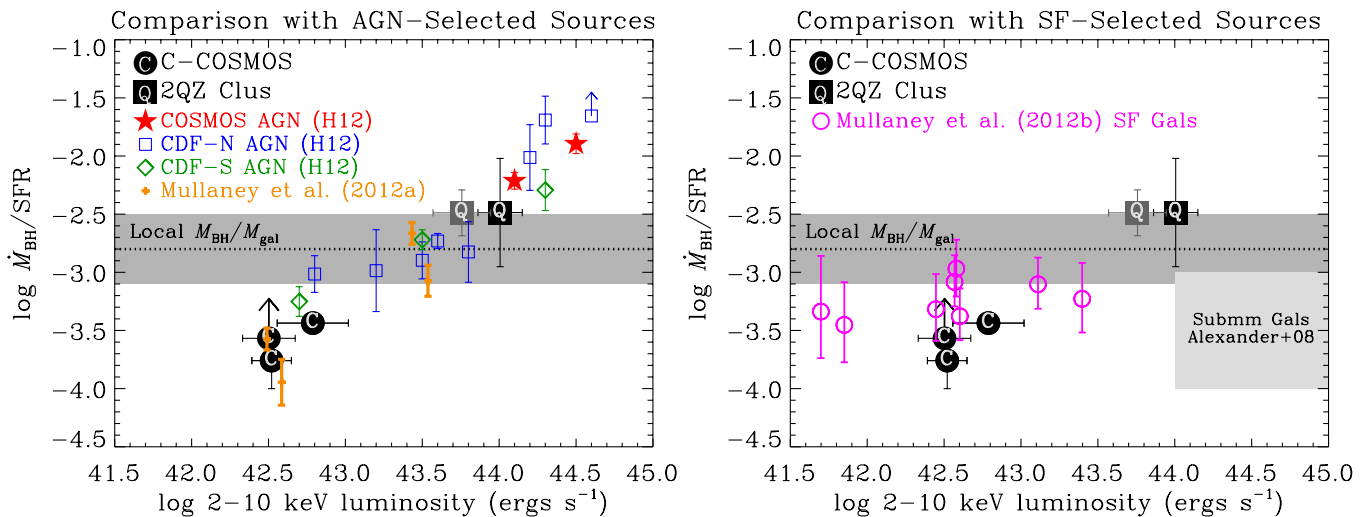
Figure 5. Mean SMBH mass accretion rate per SFR ($\dot{M}_{BH}$/SFR) vs. 2–10 keV luminosity for the stacked values of 2QZ Clus and C-COSMOS HAEs (see Table 3). In the left panel, we compare these values with $z \approx 2$ AGN-selected samples from Harrison et al. (2012; H12) and $z \approx 1$–3 AGN from Mullaney et al. (2012b). In the right panel, we compare 2QZ Clus and C-COSMOS $\dot{M}_{BH}$/SFR values with those of $z \approx 1$–2 star-forming galaxies from Mullaney et al. (2012a) and the range of vigorously star-forming submillimeter galaxies from Alexander et al. (2008). For reference, we have shown in both panels the local M_{BH}/M_{gal} relation and its dispersion as reported by Häring & Rix (2004). The 2QZ Clus HAEs have mean $\dot{M}_{BH}$/SFR values consistent with the trends observed for AGN, while the C-COSMOS HAEs appear to be broadly consistent with both the $z \approx 1$–2 AGN and star-forming galaxy populations.

(A color version of this figure is available in the online journal.)

C-COSMOS HAEs appear to have somewhat lower $\dot{M}_{BH}$/SFR values below that expected from the local M_{BH}/M_{gal} relation; however, these values appear to be consistent with those of the low-luminosity X-ray selected AGN from Mullaney et al. (2012b). Given that the mean SFRs and masses of all the AGN samples shown in the left-panel of Figure 5 are relatively high (SFR $\approx$ 10–100 $M_\odot$ yr^{-1} and $M_\star \gtrsim 5 \times 10^{10}$), this trend suggests that SMBHs and galaxies do not grow simultaneously.

In the right panel of Figure 5, we compare the 2QZ Clus and C-COSMOS HAE $\dot{M}_{BH}$/SFR values with those of $z \approx 1$–2 star-forming galaxies (Mullaney et al. 2012a). We find that the C-COSMOS HAEs have $\dot{M}_{BH}$/SFR in good agreement with field $z \approx 1$–2 star-forming galaxies, which appear to also agree with $z \approx 2$ submillimeter galaxies studied by Alexander et al. (2008). These values appear to lie a factor of ≈ 3 below the local M_{BH}/M_{gal}. We note that the various assumptions (e.g., bolometric correction and accretion efficiency) and unknown uncertainties used in our calculations may contribute to systematic offsets in $\dot{M}_{BH}$/SFR. However, if our findings are correct, typical star-forming galaxies must undergo vigorous SMBH growth in short duty cycles, where $\dot{M}_{BH}$/SFR is above the local M_{BH}/M_{gal} ratio. If the QSO phase at $L_X \gtrsim 10^{44}$ erg s^{-1} is responsible for such episodic growth, we can use our observations to estimate the QSO duty cycle required to bring star-forming galaxies onto the M_{BH}/M_{gal} relation:

$$M_{BH}/M_{gal} \approx (\dot{M}_{BH}/SFR)_{QSO} f_{QSO} + (\dot{M}_{BH}/SFR)_{gal}(1 - f_{QSO}),$$
(1)

where f_{QSO} is the fraction of time that a galaxy is in a QSO phase. Taking $M_{BH}/M_{gal} = 10^{-2.5}$–$10^{-3.0}$, $(\dot{M}_{BH}/SFR)_{QSO} \approx 10^{-1.8}$, and $(\dot{M}_{BH}/SFR)_{gal} \approx 10^{-3.3}$, we find $f_{QSO} \approx 2\%$–8%. For C-COSMOS HAEs, we estimate that the QSO fraction for $L_X \gtrsim 10^{44}$ erg s^{-1} AGN is $\approx 1.0^{+1.3}_{-0.6}\%$. This value and our duty-cycle estimate of f_{QSO} are consistent within errors, indicating that the short-term SMBH growth in a QSO phase may be sufficient to bring the typical HAE up to the M_{BH}/M_{gal} relation. This is consistent with the observation that the majority of

SMBH growth density (using X-ray emissivity as a proxy) in the universe at $z \approx 2$ can be attributed to luminous AGN ($L_X \gtrsim 10^{44}$ erg s^{-1}; e.g., Hasinger et al. 2005); a significant fraction of this population is expected to be fueled by mergers ($\approx 30\%$–40%; e.g., Treister et al. 2012). We note that none of the luminous AGN among the C-COSMOS HAEs fell within the observational footprint of the *HST* WFC3 IR-imaged region of the Cosmic Assembly Near-infrared Deep Extragalactic Legacy Survey (CANDELS; Grogin et al. 2011; Koekemoer et al. 2011), so it was not possible to examine directly the rest-frame optical morphologies of the HAE AGN subpopulation. An alternative possibility is that the apparent sequence of increasing values of $\dot{M}_{BH}$/SFR with increasing L_X is in a steady state and is due primarily to an increase in black-hole mass with increasing L_X. This explanation is supported by more recent detailed studies of local galaxies and their central SMBHs indicate M_{BH}/M_{gal} may be increasing with galaxy and SMBH mass (e.g., Graham et al. 2012; Graham & Scott 2012). Disentangling these two possibilities would require direct measurements of the galaxy and SMBH masses of the HAEs themselves. We used the *HST* ACS optical (F814W) morphology catalogs from Tasca et al. (2009) from the broader COSMOS field (Scoville et al. 2007) to compare the concentrations and asymmetries of the rest-frame UV emission from the HAEs and their AGN subpopulation. These parameters were available for 270 C-COSMOS HAEs and all 10 AGN. Compared with the C-COSMOS HAE population, the AGN subpopulation morphology distribution is skewed toward higher optical-light concentrations (K-S test reveals the populations differ at the 98.1% confidence level). The AGN subpopulation asymmetry distribution is consistent with the broader HAE population, with no evidence for more luminous AGN having larger asymmetries, as might be expected from merging systems. However, the observed *HST* images reveal that the rest-frame UV light from the most luminous AGN is dominated by the QSO emission, skewing the light to higher concentrations and making merger signatures elusive. Observations of these sources with *HST* WFC3 IR (rest-frame

optical) would improve our ability to address whether mergers play a significant role in triggering driving SMBH growth in the HAE population.

5. SUMMARY

We have conducted a $\approx$100 ks *Chandra* observation over the 2QZ Clus structure and present a *Chandra* point-source catalog. Within the *Chandra* footprint, the 2QZ Clus structure contains 21 HAEs and four QSOs at $z = 2.23$ (total of 22 unique $z = 2.23$ sources) and is on-average a factor of $\approx$2 times overdense compared to field HAEs. The 2QZ Clus was initially selected by (1) identifying an overdensity of $z \approx 2.23$ QSOs and (2) performing Hα narrow-band photometry to preferentially detect additional star-forming galaxies and AGN at $z \approx 2.23$ (via HAE selection; see Matsuda et al. 2011). Given its selection, the 2QZ Clus HAEs contain a rich mixture of AGN and star-forming galaxies. To put into broader context the 2QZ Clus HAEs, we compare their properties with those of a larger sample of 210 $z = 2.23$ HAEs selected in the C-COSMOS field. Our findings are summarized below.

1. We find seven of the 22 $z = 2.23$ sources are detected in the X-ray band, including all four QSOs. These sources have 2–10 keV luminosities of $\approx$(8–60) $\times 10^{43}$ erg s^{-1} and HB/SB count-rate ratios indicative of unobscured QSOs. Comparison with HAEs in C-COSMOS reveal that the HAE AGN fraction in the 2QZ Clus field is enhanced by a factor of $\approx 3.5^{+3.8}_{-2.2}$ compared with the broader field (after excluding pre-selected 2QZ Clus QSOs). Therefore, the 2QZ Clus structure is a region in which SMBH growth is in a particularly active phase.

2. On average, X-ray selected AGN and QSOs occupy the high-flux end of the Hα flux distribution, suggesting that the Hα line for these bright HAEs is on average dominated by the QSO component. For 2QZ Clus the mean Hα flux is higher than any non-AGN HAE, indicating that the total 2QZ Clus Hα power output for HAEs is dominated by AGN/QSO activity. However, the C-COSMOS HAEs have Hα power dominated by star-forming galaxies.

3. We find suggestive evidence that the C-COSMOS $z = 2.23$ HAE AGN fraction increases with increasing local HAE overdensity. The 2QZ Clus HAEs reside in a factor of $\approx$2 HAE overdense environment. After excluding known optically-selected QSOs, the 2QZ Clus AGN fraction is a factor of $\approx 4.1^{+5.0}_{-2.8}$ times higher than C-COSMOS HAEs in similarly overdense environments. Either the local density as measured by HAEs alone does not provide an accurate characterization of a truly more overdense 2QZ Clus environment, or the 2QZ Clus HAE population is a statistical outlier (at the $\approx$95.9% level) in terms of its elevated AGN fraction.

4. We make use of *Chandra* and *Herschel* 250 μm stacking of 2QZ Clus and C-COSMOS HAE samples to measure mean SMBH mass accretion rates and SFRs. These stacking analyses reveal that the mean X-ray emission from all HAE samples is dominated by AGN, with 2QZ Clus HAEs having QSO-like luminosities ($L_{2-10\,\mathrm{keV}} \approx$ [6–10] $\times 10^{43}$ erg s^{-1}) and C-COSMOS HAEs having much lower Seyfert-like luminosities ($L_{2-10\,\mathrm{keV}} \approx$ [3–6] $\times 10^{42}$ erg s^{-1}). The mean SFRs range from $\approx$60–110 $M_\odot$ yr^{-1} for 2QZ Clus HAEs depending on whether or not optically-selected QSOs are removed. The SFRs for C-COSMOS HAEs span $\lesssim$40 $M_\odot$ yr^{-1} to $\approx$70 $M_\odot$ yr^{-1}. The inferred mean SMBH mass accretion rate to SFR ratio ($\dot{M}_{\mathrm{BH}}$/SFR) for these samples indicate that the 2QZ Clus SMBHs and galaxies appear to be growing at rates comparable to those expected by the local $M_{\mathrm{BH}}/M_{\mathrm{gal}}$ ratio, while the mean $\dot{M}_{\mathrm{BH}}$/SFR for C-COSMOS HAEs lie a factor of $\approx$3 times lower than the local $M_{\mathrm{BH}}/M_{\mathrm{gal}}$ ratio. We find that the $\dot{M}_{\mathrm{BH}}$/SFR versus X-ray luminosity for both the 2QZ Clus and C-COSMOS HAE samples appear to follow trends found for $z \approx 1$–2 star-forming galaxies and $z \approx 2$ X-ray selected AGN.

5. We estimate that an episodic QSO phase with a duty cycle of $\approx$2%–8% would allow C-COSMOS HAEs to emerge onto the $M_{\mathrm{BH}}/M_{\mathrm{gal}}$ relation despite their lower population-averaged $\dot{M}_{\mathrm{BH}}$/SFR. This estimate is consistent with the observed C-COSMOS HAE AGN fraction ($\approx$0.4%–2.3%) for $L_{\mathrm{X}} \gtrsim 10^{44}$ erg s^{-1} sources.

Future observations of the 2QZ Clus are needed to further evaluate (1) what physical conditions have led to such an enhanced AGN fraction, (2) the large-scale environment of the 2QZ Clus structure, and (3) whether there is a significant underlying overdensity of galaxies that are not HAEs (e.g., massive passive galaxies and additional galaxies with low SFRs or heavily extinguished Hα emission).

REFERENCES

Adelman-McCarthy, J. K., Agüeros, M. A., Allam, S. S., et al. 2008, ApJS, 175, 297
Alexander, D. M., Brandt, W. N., Smail, I., et al. 2008, AJ, 135, 1968
Basu-Zych, A. R., Lehmer, B. D., Hornschemeier, A. E., et al. 2013, ApJ, 762, 45
Bell, E. F., Papovich, C., Wolf, C., et al. 2005, ApJ, 625, 23
Bennert, V. N., Auger, M. W., Treu, T., Woo, J.-H., & Malkan, M. A. 2011, ApJ, 726, 59
Best, P. N., Kauffmann, G., Heckman, T. M., et al. 2005, MNRAS, 362, 25
Bower, R. G., Benson, A. J., Malbon, R., et al. 2006, MNRAS, 370, 645
Bower, R. G., McCarthy, I. G., & Benson, A. J. 2008, MNRAS, 390, 1399
Calzetti, D. 1997, AJ, 113, 162
Chary, R., & Elbaz, D. 2001, ApJ, 556, 562
Civano, F., Elvis, M., Brusa, M., et al. 2012, ApJS, 201, 30
Croom, S. M., Smith, R. J., Boyle, B. J., et al. 2001, MNRAS, 322, L29
Croom, S. M., Smith, R. J., Boyle, B. J., et al. 2004, MNRAS, 349, 1397
Croton, D. J., Springel, V., White, S. D. M., et al. 2006, MNRAS, 365, 11
Daddi, E., Cimatti, A., Renzini, A., et al. 2004, ApJ, 617, 746
De Lucia, G., Springel, V., White, S. D. M., Croton, D., & Kauffmann, G. 2006, MNRAS, 366, 499
Digby-North, J. A., Nandra, K., Laird, E. S., et al. 2010, MNRAS, 407, 846
Efstathiou, A., & Rowan-Robinson, M. 1995, MNRAS, 273, 649
Ehlert, S., Allen, S. W., Brandt, W. N., et al. 2013, MNRAS, 428, 3509
Elbaz, D., Daddi, E., Le Borgne, D., et al. 2007, A&A, 468, 33
Elvis, M., Civano, F., Vignali, C., et al. 2009, ApJS, 184, 158
Fanidakis, N., Baugh, C. M., Benson, A. J., et al. 2012, MNRAS, 419, 2797
Geach, J. E., Alexander, D. M., Lehmer, B. D., et al. 2009, ApJ, 700, 1
Geach, J. E., Smail, I., Best, P. N., et al. 2008, MNRAS, 388, 1473
Geach, J. E., Sobral, D., Hickox, R. C., et al. 2012, MNRAS, 426, 679
Gehrels, N. 1986, ApJ, 303, 336
Governato, F., Baugh, C. M., Frenk, C. S., et al. 1998, Natur, 392, 359
Graham, A. D., & Scott, N. 2012, arXiv:1211.3199
Graham, A. W., Spitler, L. R., Forbes, D. A., et al. 2012, ApJ, 750, 121
Grogin, N. A., Kocevski, D. D., Faber, S. M., et al. 2011, ApJS, 197, 35
Häring, N., & Rix, H.-W. 2004, ApJL, 604, L89
Harrison, C. M., Alexander, D. M., Mullaney, J. R., et al. 2012, ApJL, 760, L15

Hasinger, G., Miyaji, T., & Schmidt, M. 2005, A&A, 441, 417
Hatziminaoglou, E., Omont, A., Stevens, J. A., et al. 2010, A&A, 518, L33
Hornschemeier, A. E., Brandt, W. N., Garmire, G. P., et al. 2001, ApJ, 554, 742
Kauffmann, G. 1996, MNRAS, 281, 487
Koekemoer, A. M., Faber, S. M., Ferguson, H. C., et al. 2011, ApJS, 197, 36
Kroupa, P. 2001, MNRAS, 322, 231
Lehmer, B. D., Alexander, D. M., Bauer, F. E., et al. 2010, ApJ, 724, 559
Lehmer, B. D., Alexander, D. M., Chapman, S. C., et al. 2009a, MNRAS, 400, 299
Lehmer, B. D., Alexander, D. M., Geach, J. E., et al. 2009b, ApJ, 691, 687
Lehmer, B. D., Brandt, W. N., Alexander, D. M., et al. 2008, ApJ, 681, 1163
Marconi, A., Risaliti, G., Gilli, R., et al. 2004, MNRAS, 351, 169
Martini, P., Sivakoff, G. R., & Mulchaey, J. S. 2009, ApJ, 701, 66
Matsuda, Y., Smail, I., Geach, J. E., et al. 2011, MNRAS, 416, 2041
McNamara, B. R., & Nulsen, P. E. J. 2012, NJPh, 14, 055023
Mullaney, J. R., Alexander, D. M., Goulding, A. D., & Hickox, R. C. 2011, MNRAS, 414, 1082
Mullaney, J. R., Daddi, E., Béthermin, M., et al. 2012a, ApJL, 753, L30
Mullaney, J. R., Pannella, M., Daddi, E., et al. 2012b, MNRAS, 419, 95
Netzer, H., Lutz, D., Schweitzer, M., et al. 2007, ApJ, 666, 806
Oliver, S. J., Bock, J., Altieri, B., et al. 2012, MNRAS, 424, 1614
Page, M. J., Symeonidis, M., Vieira, J. D., et al. 2012, Natur, 485, 213
Puccetti, S., Vignali, C., Cappelluti, N., et al. 2009, ApJS, 185, 586
Salim, S., Rich, R. M., Charlot, S., et al. 2007, ApJS, 173, 267
Scoville, N., Abraham, R. G., Aussel, H., et al. 2007, ApJS, 172, 38
Sobral, D., Best, P. N., Geach, J. E., et al. 2009, MNRAS, 398, 75
Sobral, D., Smail, I., Best, P. N., et al. 2013, MNRAS, 428, 1128
Spergel, D. N., Verde, L., Peiris, H. V., et al. 2003, ApJS, 148, 175
Steidel, C. C., Adelberger, K. L., Dickinson, M., et al. 1998, ApJ, 492, 428
Steidel, C. C., Adelberger, K. L., Shapley, A. E., et al. 2005, ApJ, 626, 44
Tasca, L. A. M., Kneib, J.-P., Iovino, A., et al. 2009, A&A, 503, 379
Treister, E., Schawinski, K., Urry, C. M., & Simmons, B. D. 2012, ApJL, 758, L39
Vasudevan, R. V., & Fabian, A. C. 2007, MNRAS, 381, 1235
Volonteri, M., Haardt, F., & Madau, P. 2003, ApJ, 582, 559
Xue, Y. Q., Brandt, W. N., Luo, B., et al. 2010, ApJ, 720, 368